Blue laser welding of multi-layered AISI 316L stainless steel micro-foils

Abhishek Das[a,*], Robert Fritz[b], Mathew Finuf[b], and Iain Masters[a]

[a]WMG, The University of Warwick, Coventry, CV4 8GJ, United Kingdom

[b]NUBURU Inc., 7442 S. Tucson Way, Centennial, CO, 80112, USA

[*]E-mail: A.Das.1@warwick.ac.uk

Abstract:

This paper investigates the microstructural and mechanical behaviour of overlap micro-joints produced by a blue laser system with a wavelength of ~450 nm. AISI 316L stainless steel was used to produce assemblies of 20 layers of 25 µm micro-foil welded to a single 200 µm foil. The welding speed was varied from 6.5 m/min to 9.5 m/min in incremental steps of 1.0 m/min whilst the power was kept at a maximum output level of 500W. The joints were analysed for fusion zone microstructure, crystallographic grain structure, microhardness distribution and lap shear and T-peel strengths. Interface width and penetration depth were used as key quality indicators to characterise the fusion zone microstructure. The welding speed modulation indicated that the penetration depth can be easily controlled during blue laser welding. The mechanical strength was evaluated by performing lap shear and T-peel tests. The results indicated that the blue laser welding can have a considerable impact on weld geometry and joint strength as it can reduce discontinuities in welded regions and generate good mechanical properties. This study demonstrated for the first time that the blue laser can be successfully implemented for multiple stack-up joining of stainless steel.

Keywords: Blue laser welding; stainless steel; thin foils; weld microstructure; tensile performance

1. Introduction

In many industrial applications, materials are exposed to elevated temperatures or corrosive environments necessitating appropriate material selection to prevent chemical degradation. Additionally, formability is also needed to make desired shapes. Often industrial parts and components are covered with corrosion-resistant materials including thin foils of stainless steel thin foils, tantalum or Ni alloys [1]. As a result, there is a growing need for micro-welding of thin foils. Laser welding is expected to be the preferred micro joining method as it allows precise heat control compared with others processes and reduces the size of the heat-affected zone (HAZ), residual stress and the presence of discontinuities [1, 2].

1.1. Industrial requirements

One of the major challenges for the 21st century is the long-term impact of greenhouse gases on global climate. This drives the need for usage and storage of alternative energy to reduce the generation of greenhouse gases [3]. Automotive vehicles running on fossil fuels remain one of the main contributors to greenhouse gas emissions [4]. 12% of total carbon dioxide (CO_2) emissions are generated by automotive vehicles [5]. It has been reported that nearly 21% of the

European Unions' total emissions of carbon dioxide (CO_2), the main greenhouse gas, in 2016 [6] was attributable to road transport. Under these alarming circumstances, various national and international legislative authorities are setting out stringent emission targets to reduce greenhouse gas generation for all surface transport vehicles, especially for automotive vehicles [4, 7]. However, with continually growing energy needs, energy storage, including high capacity batteries and supercapacitors, is the technology of choice [8-10]. Energy storage devices are used as alternative power sources for electric vehicles or hybrid/ plug-in hybrid electric vehicles as well as in telecommunications and for standby power systems. There is, therefore, great emphasis on the research and development of energy storage technologies including the development of new electrochemistries for batteries or capacitors [8]. Copper and aluminium are the traditional materials used for electrodes, however, stainless steel is being investigated for emerging battery/supercapacitor technologies where the cell chemistry is incompatible with Cu and Al. As a part of this new electrochemistry development, a few active materials chemical compositions require the use of stainless steel as an electrode carrier [11]. As a result of this changing need, an efficient joining technique is required to join multiple stainless steel foils together. At present, various joining techniques are used to weld batteries or supercapacitors including ultrasonic welding, ultrasonic wedge bonding, pulsed TIG spot welding, resistance spot/projection welding, micro-clinching, soldering, laser welding and mechanical assembly [12-14]. For multiple sheet welding of soft materials, ultrasonic welding is preferred and used for welding tabs/busbars made of copper, aluminium or nickel [15, 16]. However, traditional joining methods, such as mechanical or ultrasonic bonding, are no longer adequate for the higher power demands of modern batteries which require the use of harder materials like stainless steel. In contrast, laser welding can be used for welding multiple stainless steel foils and has the added advantages of non-contact joining, high production rate, high flexibility, weight reduction, lower energy requirements and lower cost [17, 18]. The commonly used high-power industrial lasers operate at infrared (IR) wavelengths (typically 1064 nm) but for battery welding applications have the disadvantages high spatter, porosity and defects giving the potential for large mechanical and electrical variability. Blue light lasers (wavelength ~ 450 nm) have now been developed [19] and much higher energy absorption on highly reflective surfaces. The variation of absorptivity with wavelength for various metals was reported within the literature [20, 21]. For example, the absorptivity values at blue wavelength are around 13, 3, 1.5, and 1.3 times higher than at IR wavelength for copper, aluminium, nickel, and steel, respectively [22-24]. This reduces the amount of energy which must be put into the weld, reducing both the tendency to spatter and the creation of voids during keyhole welding operations. This widens the processing window and produces welds with improved mechanical strength and lower electrical resistivity by enhancing the weldability of highly conductive and reflective materials. Blue laser joining is to be investigated further for energy storage applications.

1.2. Research gap and objectives

Bead on plate welding was applied using 1 kW CO_2 laser on a 316L stainless steel sheet of 1 mm thickness to study the microstructural behaviour by Kell, et al. [25]. They found that the weld metal formed significantly larger grains (around 200 µm) compared to 20 µm of base

metal. Alloying element losses during pulsed laser welding of 316 stainless steel was studied by Jandaghi, et al. [26] and they concluded that the Mn and Cr concentrations were reduced within the weld metal while the percentage of Fe, Ni were increased simultaneously. Few studies reported on butt configuration using stainless steel 316 [27, 28] where the various thicknesses of sheet combinations were studied. However, in case of overlap joint configuration, the reported work on stainless steel foils is mainly focused on single-layer welding with inferred (IR) wavelength lasers. Using a direct diode laser, stainless steel micro-welding was conducted by Abe, et al. [2] and the tensile strength of the welded foil was nearly equal to the nominal value of the base material. Similarly, Ventrella, et al. [1] studied single layer based overlap joint using pulsed neodymium: yttrium aluminum garnet laser considering 100 µm thin foil of AISI 316L stainless steel. They reported the feasibility of joining AISI 316 stainless steel using IR laser and weld geometric quality such as bead width, connection width and bead depth were increased with pulse energy, and then decreased at the end because of burn-through. Their extended study in [29] used pulsed laser welding to weld 100 µm thin foil to 3 mm thick sheet. Penetration depth was increased with increasing pulse energy and the lap shear strength initially increased and then decreased as the pulse energy increased. An initial increase in pulse energy created larger melt pool which elevated the quality of the weld from under-weld to good-weld, however, further increase in pulse energy slowly moved from good-weld to over-weld which decreased the lap shear strength. Kim, et al. [30] also investigated the effect of beam size on weldability of a 50 µm-thick stainless steel foil onto a 1 mm-thick stainless steel sheet. They found that the effect of beam diameter was significant in the ultra-thin foil welding, and a smaller spot size was highly recommended. For larger beams, the surface tension effect became too large to sustain a stable weld pool. Tensile strength and hardness were found to be inversely proportional to the penetration depth. Pakmanesh and Shamanian [31] studied laser welding parameters on the lap-joint of a 316L stainless steel foil using a spot size of 0.2 mm when two metal foils were welded together. They reported that the most important parameter affecting underfill and undercut was the laser power, whose effect was 65%. The studies conducted on stainless steel thin foil welding are typically based on two layers lap weld using IR laser. But, for the energy storage applications, it needs multiple thin foils welding. Therefore, this paper explores, for the first time, the weldability of blue laser joining when 20 layers of 25 µm multiple thin stainless steel foils welded with another 200 µm stainless steel foil. The research work reported in the literature and identified research gap are summarised in Table 1.

Table 1 Research studies reported in the literature and identified research gap to be addressed in this paper.

For stainless steel micro joining	Two layers based overlap joint	Multiple layers based overlap joint
IR laser	Abe, et al. [2] Ventrella, et al. [1] Kim, et al. [30] Pakmanesh and Shamanian [31]	-
Blue laser	-	*To be addressed in this paper*

The aforesaid research gap is addressed in this paper by fulfilling the following objectives: (i) to evaluate the fusion zone geometries and key characteristics, (ii) to investigate details fusion zone microstructure using electron backscatter diffraction (EBSD) maps, (iii) to determine the microhardness distributions from base material to fusion zone, and (iv) to perform the lap shear strength and T-peel strength analysis on the welded overlap joints.

2. Materials and experimental procedures

2.1. Details of Materials and joint configuration

In this blue laser investigation, 20 layers of 25 µm stainless steel foils are welded with 200 µm stainless steel tabs of AISI 316L grade. The chemical composition of the AISI 316L base material used in this study is listed in Table 2. The base materials of both thicknesses were cut to a size of 100 mm × 25 mm and thereafter, 20 layers of 25 µm thin foils were placed over the single layer of 200 µm thick foil with an overlap of 25 mm. The schematic of the lap shear and T-peel test specimen configurations with 15 mm long blue laser welded joint is shown in Figure 1. The measured average 0.2% proof stress, tensile stress at maximum load (i.e. UTS), and elongation were 274 MPa, 549 MPa, 2732 N and 17.7% respectively.

Table 2 Chemical composition (wt %) of AISI 316L stainless steel used in this study [1, 32].

Alloy Grade	Cr	Ni	Mn	Cu	Si	C	Nb	P	S	Mo	Fe
AISI 316L	16.7	11.6	1.7	0.05	0.3	<0.03	0.03	0.025	0.003	2.4	Remaining

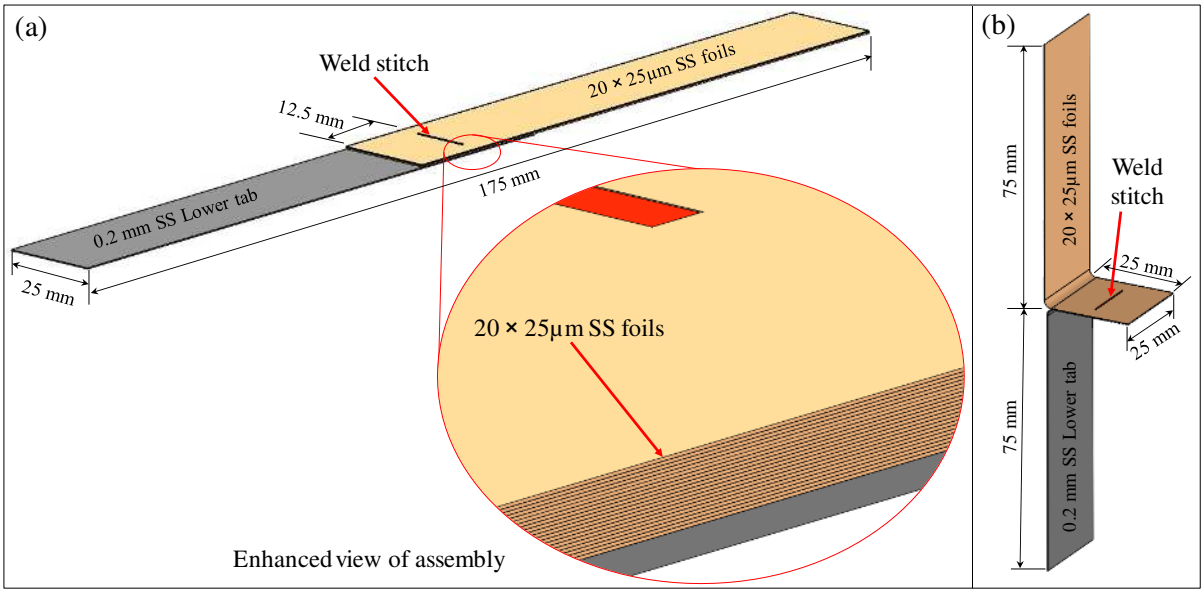

Figure 1 Schematic of multi-layered joint configuration (a) lap shear joint with an enhanced stack-up view, and (b) T-peel joint.

2.2. Blue laser system

The blue laser system used for this study was a Nuburu AO-500 designed to provide 500 W power with continuous wave (CW) mode at a blue light wavelength of ~450 nm. The laser optics were mounted on an X-Y gantry system and the spot size at the focus was approximately 200 µm in diameter. The focus point was fixed on the top surface of stainless steel foils and the laser beam was perpendicular to the surface. The joining trials were performed in a shielding gas environment using Argon (Ar) at a flow rate of 20 L/min through a 3 mm nozzle, as the blue laser set-up shown in Figure 2(b). Absence of intimate contact may lead to unwanted quality including undercut, porosity, no joint or upper material cutting [33]. Therefore, fixturing is important for laser welding, especially for joining thin foils. To ensure required joint fit-ups, tolerances were held strictly without allowing either mismatch or gaps [34]. A special set of fixtures was developed to ensure part-to-part intimate contact and avoid excessive deformation during welding, as shown in Figure 2(a). As the maximum attainable power of the blue laser system was 500W, the laser power was fixed at the maximum level where the welding speed was varied from 6.5 m/min to 9.5 m/min with an incremental step size of 1.0 m/min as shown in Table 3. The experimental results were analysed on the basis of the relationship between welding speed and the key geometric characteristics of the fusion zone, especially the penetration depth variation and mechanical strength. The specimens were prepared and cleaned with acetone to ensure that all samples presented the same surface conditions with a homogeneous finish.

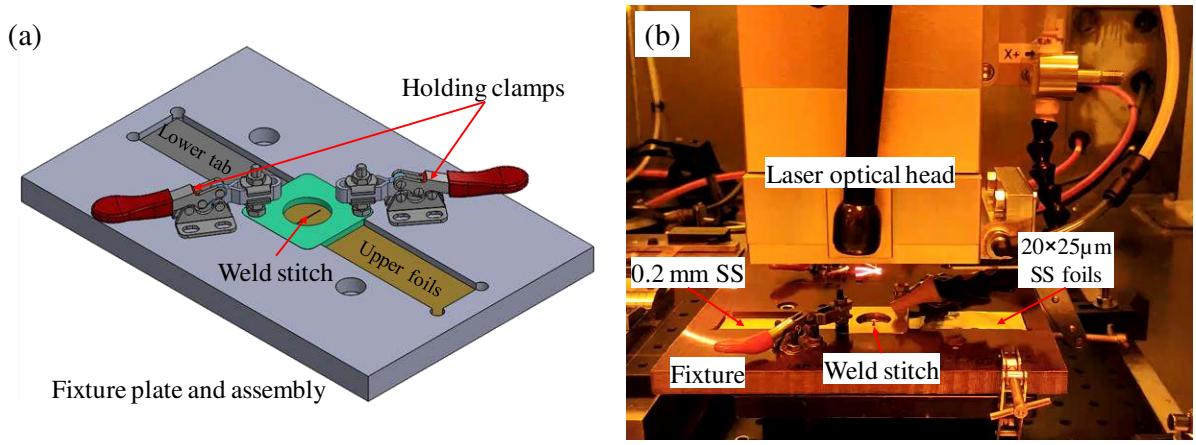

Figure 2 (a) Schematic of the fixture used to make joints, and (b) blue laser welding set-up.

Table 3 Joining parameters used for AISI 316L stainless steel foil welding.

Exp ID	Laser Power (W)	Welding speed (m/min)
1	500 (using AO-500 blue laser)	6.5
2		7.5
3		8.5
4		9.5

2.3. Details of specimen preparation and test conditions

After carrying out the blue laser welding, samples were prepared for metallographic inspection and subsequent mechanical strength evaluation. To investigate the fusion zone, metallographic samples were cut perpendicular to the welding direction using a precision cutter and then, they were cold mounted using epoxy mounting resin and hardener. The mounted samples were ground and subsequently polished using 9 µm and 3 µm diamond suspension solutions, and thereafter, 0.02–0.06 µm colloidal silica solution as the final stage of polishing. To obtain the microstructure of base material and fusion zone, the polished samples were electrolytically etched (5V, 10 sec) with a 50% nitric acid solution. Using a Nikon Eclipse LV150N optical microscope, the weld microstructures were examined and the penetration depth and interface width recorded. Microhardness profiles were measured using 200 gf load and a test duration of 10s. A Carl Zeiss Sigma scanning electron microscopy (SEM) equipped with field emission gun was used for energy dispersive spectroscopy (EDS) and EBSD analysis. The lap shear and T-peel tests were performed using an Instron 3367 static test frame with a 30 kN load capacity and cross-head speed of 2 mm/min and 10 mm/min, respectively (adapted from [15, 35]). The peak loads obtained from the lap shear and T-peel tests were recorded to evaluate the mechanical strength of the weld and further used as a measure of weld performance. For each test condition, three samples were prepared for inspection of the weld geometry and measurement of the tensile strength to obtain consistent and reliable results.

3. Results and discussion

3.1. Joint fusion zone characteristics

The weld fusion zone microstructures of the overlap joints at varying welding speed are plotted in Figure 3. Using the optical microscope, the key geometrical characteristics (such as penetration depth and interface width) were measured and plotted in Figure 4. It is evident from these cross-sectional micrographs that they were composed of two distinctive regions, namely, the fusion zone (FZ) and base material (BM). Due to the application of laser energy at blue wavelength, the 20 layers stainless steel foils and lower sheet at the point of laser beam application were melted and then resolidified together to form the fusion zone. Overall good surface appearance was observed and no detectable defect was noticed on the top surface of the weld stitch or adjacent areas for all the investigated welding conditions. No cracks or discontinuities were observed in any of the welds which can be attributed to good crack resistance of the base metal, low spatter blue laser welding and suitable fixturing with correct process parameters. Therefore, it demonstrated the combined benefits of the blue laser welding with shielding gas to prevent oxidation, large porosities and gas inclusions. In general, laser welding without shielding gas gives rise to weld embrittlement and poor formability due to the presence of oxide layers [36]. Figure 3 confirms that the blue laser welding was conducted in keyhole mode for all the welding speeds where the laser energy was absorbed by the top foil, and subsequently transferred into the lower foils as the molten weld pool developed. Microstructural inspection revealed clear columnar grain growth from the fusion boundary (i.e. transition from BM to FZ) towards the centre of the fusion zone as a result of keyhole welding. For example, Figure 3(c) shows the transition from the base material and grain growth direction

toward the fusion zone. It is evident from Figure 3 that the fusion zone morphology was symmetrical about the axis of the laser beam.

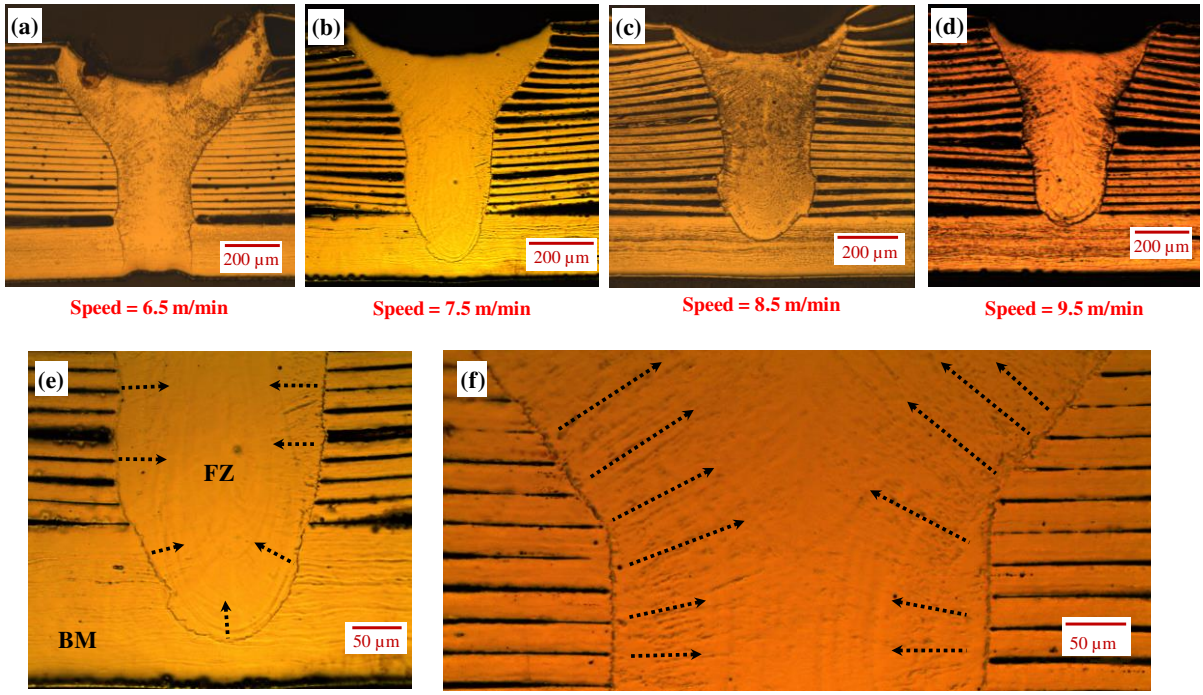

Figure 3 Weld fusion zone microstructures at varying welding speed (a) 6.5 m/min, (b) 7.5 m/min, (c) 8.5 m/min, (d) 9.5 m/min, (e) enhanced view of fusion zone at lower base material from 7.5 m/min, (f) enhanced view of fusion zone with the thin foils from 6.5 m/min where arrows showing the fusion zone grain orientation.

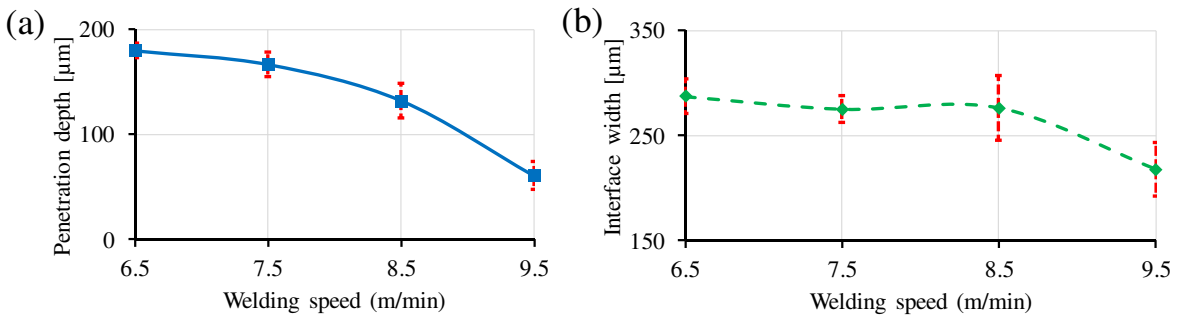

Figure 4 The relationship between key geometric characteristics and welding speed (a) penetration depth, and (b) interface width.

One of the key geometrical characteristics, penetration depth showed a decreasing trend with increasing welding speed due to a reduction in energy input, as shown in Figure 4(a). For example, the welding speed of 6.5 m/min equated to an energy input of 4.62 J/mm and gradually reduced to 3.16 J/mm when the speed increased to 9.5 m/min. Due to this reduction in energy input as well as a change in laser – metal interaction time, a major change in penetration depth was observed. At higher energy input, a larger volume of material was melted propagating through the base material resulting in full penetration. Therefore, a full penetration was observed at 6.5 m/min which can be categorised as ‘over-weld’ whereas welding at 9.5

m/min penetration was only 60.9 µm which is classed as an 'under-weld'. To avoid full penetration or under-weld conditions, welding at 7.5 m/min and 8.5 m/min was preferred and can be categorised as 'good-weld'. The average penetration depths were 166.9 µm and 132.4 µm obtained from welding speed of 7.5 m/min and 8.5 m/min respectively. These results indicated that weld pool characteristics, especially penetration depth, are sensitive to the variation in energy input resulting from the change in welding speed. In contrast, no large change in interface width was obtained due to the change in welding speed as shown in Figure 4(b). For example, average interface width was around 280 µm for welding speeds from 6.5 m/min to 8.5 m/min and a slight reduction was obtained at 9.5 m/min (i.e. 217.7 µm) due to under-weld. Although the weld fusion zone geometry confirmed that all welding was conducted in keyhole mode. No welding cracks were observed in any of the welds accompanied with no or little porosity in the order of magnitude less than 10 µm. This suggests that the blue laser was suitable for multi-layered micro-foils welding of AISI 316L stainless steel. One of the good-welds from welding speed of 7.5 m/min was selected for additional microstructural-crystallographic characterisation and micro-hardness analyses.

The EBSD image provided vital information on the fusion zone grain distribution and formation of grains from base material to the fusion zone. The base materials and the crystallographic orientation of grains from welding at 7.5 m/min are shown in Figure 5. The base material images are shown in Figure 5(a) and (b). The average grain size of 25 µm and 200 µm foils were 6 µm and 19.5 µm. The inspected surface for EBSD measurement is shown in Figure 5(d). The crystallographic orientation map obtained from the EBSD represents the details of grain size distribution and their orientation across the weld zone (i.e. from the base material to fusion zone). A distinct boundary was observed between the base material and fusion zone where a sharp change in grain size occurs. The inverse pole map, shown in Figure 5(c), reveals the columnar grain formation from base material to the centre of the weld with equiaxed grains resulted at the centre. The enhanced views of fusion zone are shown in Figure 5(e)-(g) including the transition of 25 µm thin foils to fusion zone, 200 µm thick foil to fusion zone and equiaxed grains at the centre of the columnar grains merging from both directions. These grain orientation and columnar formations were the results of the cooling of the fusion zone where heat was mainly conducted away from the molten material to the base material. The columnar grain size generally increased from the bottom to the top of the fusion zone. The grains at the bottom of the fusion zone were of 60 µm whereas grains at middle and top of the fusion zone were around 80 µm and 102 µm respectively. This type of grain formation and microstructure were expected due to the high cooling rate which is typical of the laser welding process. This grain formation is determined by the ratio of the temperature gradient (G) to grain growth rate (R) during solidification [37]. Columnar grain growth is expected when the G/R ratio is high. During the solidification, the grain growth was nearly perpendicular to the fusion zone boundary. The un-melted grains at the fusion boundary were acted as nucleation sites for the fusion zone columnar grains (epitaxial growth).

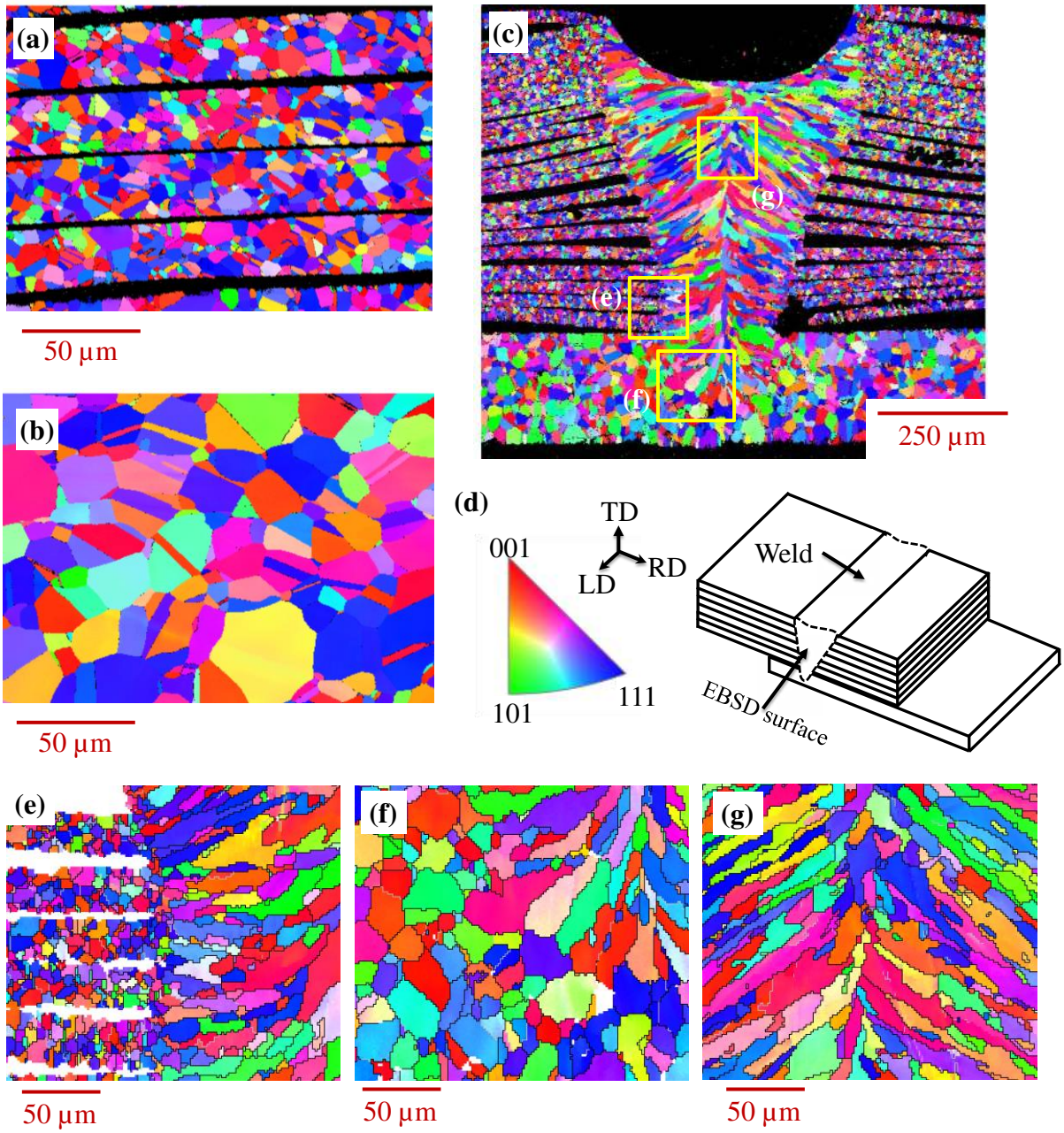

Figure 5 Electron backscatter diffraction (EBSD) maps of (a) base material of 25 µm multiple micro-foils, (b) 200 µm lower base material, (c) fusion zone grain distribution, and (d) unit triangle of the inverse pole figure showing the crystal alignment and schematic geometry showing EBSD measured surface, (e) – (f) enhanced views of different regions in the fusion zone.

3.2. Joint micro-hardness profile

Microhardness tests were performed to identify possible effects of microstructural heterogeneities in the fusion zone, heat affected zone and base material. To map the microhardness within the fusion zone and base material, three microhardness profiles were defined (i) Profile 1: microhardness distribution at the upper side of the fusion zone, (ii) Profile 2: microhardness changes from top to bottom within the fusion zone, and (iii) Profile 3:

microhardness profile in the 0.2 mm lower sheet distributed from the fusion zone to either side of the base material. The microhardness profiles obtained from the good-weld condition (i.e. welding at 7.5 m/min) are shown in Figure 6 with their measurement locations indicated on the welded geometry.

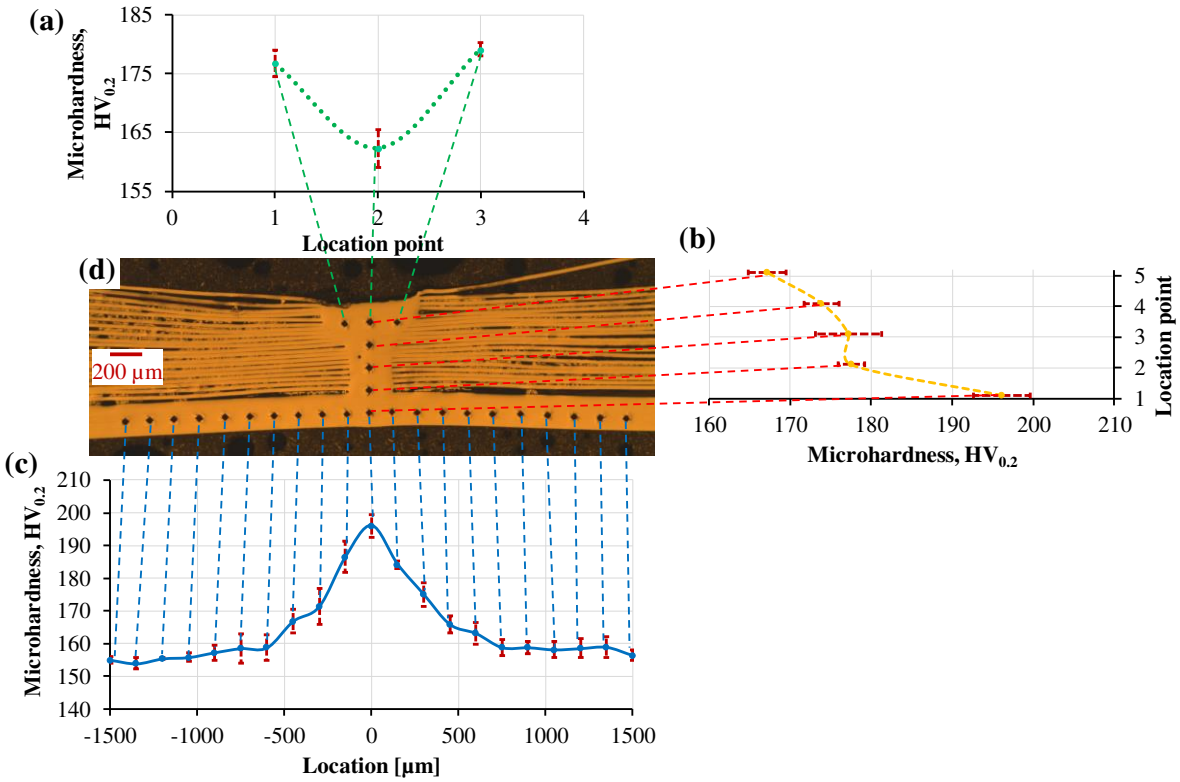

Figure 6 Microhardness profiles of fusion zone and lower base material obtained from 7.5 m/min welding condition (a) at the upper side of the fusion zone, (b) vertical distribution within the fusion zone, (c) lower base material and fusion zone, and (d) optical map of the hardness measurement points.

The horizontal microhardness distribution within the fusion zone, (profile 1) shown in Figure 6(a), revealed that the average hardness at the centre of the weld was comparatively lower (approximately 10%) than both sides. It is well known, that the material hardness is closely related to the grain size according to Hall-Patch principle where larger grain formation results in a large contribution to the hardness loss of the fusion zone and neighbouring area Sun, et al. [38]. From the optical images and EBSD maps, it was observed that the columnar grains were resulted from both sides of the fusion zone interface and grew towards the centre of the weld. However, equiaxed grains were formed at the centre of the weld in between the columnar grains. Additionally, the cooling of the molten weld pool started from the fusion zone boundary toward the centre of the weld pool. Due to these grain distribution and cooling rate difference, the hardness was relatively higher at the fusion zone boundary regions than the centre. In general, the fusion zone exhibits a variety of significant alloying elements including Mn, Cr, Ni and Fe. The EDS analysis results obtained from the middle of the fusion zone and base material are shown in Figure 7. The concentrations of iron and chromium in the weld metal were increased whereas the concentrations of nickel and manganese were decreased. Similar

observations were made in the literature after the IR laser welding of stainless steel 316 [26, 27]. However, the average hardness was increasing when moving from the top of the fusion zone to the bottom as shown in Figure 6(b). This vertical hardness profile shows that the average microhardness at the top of the fusion zone was 162.17 $HV_{0.2}$ and slowly increasing to 196.1 $HV_{0.2}$ at the bottom of the fusion zone-base metal interface. The maximum hardness change was observed in the 0.2 mm bottom sheet when measured from the centre of the fusion zone to the base material. The average microhardness within the base material was 156.6 $HV_{0.2}$. The maximum microhardness was 196.1 $HV_{0.2}$ at the fusion zone-base metal interface, as shown in Figure 6(c). This profile 3 confirms that the microhardness values started to drop from the central location towards the base material and settled to average base material microhardness. This increase in microhardness close to the fusion zone was due to the heat-affected zone. This was expected because the mechanical properties of steel, in general, were based on its microstructure where some intergranular precipitates can be present [27].

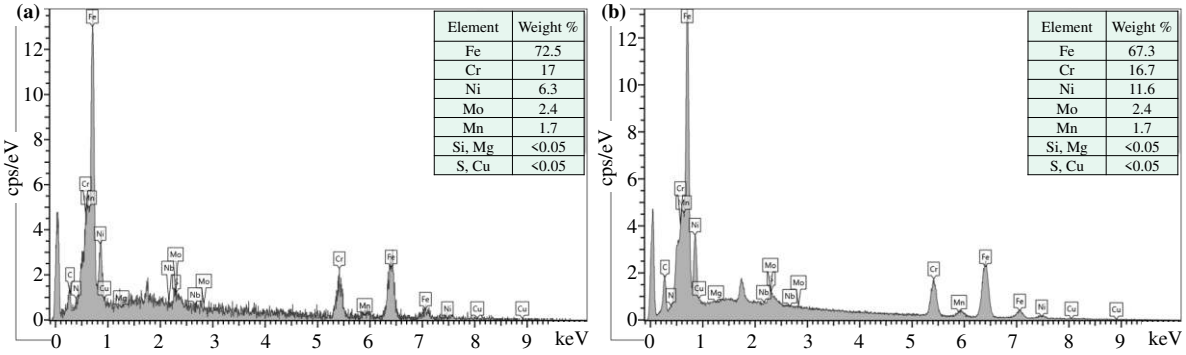

Figure 7 EDS analysis for main alloying elements (a) fusion zone, and (b) base material obtained from 7.5 m/min welding condition.

3.3. Joint strength and failure mode characterisation

After carrying out the experimental runs as per the parameters listed in Table 3, the maximum lap shear and T-peel loads were used to evaluate joint strength. The lap shear and T-peel strength variation with the welding speed are shown in Figure 8. A negative correlation was observed between lap shear load and welding speed. An incremental increase in welding speed brought down the maximum lap shear load. From the metallographic inspection, it was confirmed that full penetration of the lower sheet occurred at 6.5 m/min and the penetration depth gradually reduced with increasing speed resulting in an under weld at 9.5m/min. As the welding power was fixed at 500W, the higher welding speed meant less time for the laser-metal interaction and less energy input. For example, when the welding speed increased from 6.5 m/min to 9.5 m/min, around 42 % reduction in lap shear load was observed due to low penetration depth. Similar decreasing behaviour with welding speed was observed with the maximum T-peel load. A small increase in T-peel load occurred when the welding speed moved from 6.5 m/min to 7.5 m/min, but thereafter the load gradually decreased. The lowest T-peel strength of 618.75 N was obtained at 9.5 m/min which was approximately 51% lower to the maximum T-peel strength of 1263.2 N obtained at 7.5 m/min. In both lap shear and T-peel tests, the lowest values were obtained at 9.5 m/min welding speed due to low or

intermittent penetration of the fusion zone. Similar to these, *while laser welding thin materials*, Ventrella, et al. [1] found that lap shear strength increased with penetration depth due to increase in pulse energy, however, further increase in pulse energy created under filling leading to over-weld and subsequently reduced the lap shear strength. In contrast, *while joining thin to thick combination*, Ventrella, et al. [29] and Kim, et al. [30] concluded that the tensile strength was inversely proportional to the penetration depth as increasing penetration depth created the over-weld condition.

The failure modes obtained from both the lap shear and T-peel strength can be classified into two distinctive categories which were (i) partial circumferential fracture with material tear – failure occurred at the base material instead of joint and then the fracture propagated with lower material tear keeping the joint intact, and (ii) interfacial separation with partial adhesion – the failure occurred inside the weld fusion zone with partial adhesion of lower materials and subsequent lower material tear. The failure modes obtained from the lap shear and T-peel tests are shown in Figure 9 and also highlight the two failure modes. In general, failure initiates from two weak positions around the joint which are located at (a) the boundary between the fusion zone and base material, and (b) interface between the upper and lower materials. The failure mode and strength of the joint are mainly related to the strength of these two positions that are mainly affected by the penetration depth, interface width and microstructure gradient. As a result, partial circumferential fracture with a material tear was obtained from the lower welding speed range (i.e. 6.5 m/min and 7.5 m/min) due to good penetration depth whereas interfacial separation with partial adhesion resulted from high welding speeds (i.e. 8.5 m/min and 9.5 m/min) due to low penetration depth and interface width.

Comparing the joint strength with the failure mode characteristics, it can be concluded that higher strength combined with a partial circumferential fracture with a material tear was the preferred joint. At higher welding speed, interfacial separation with partial adhesion was obtained due to low energy input and resulting in poor propagation of the weld pool into the lower material.

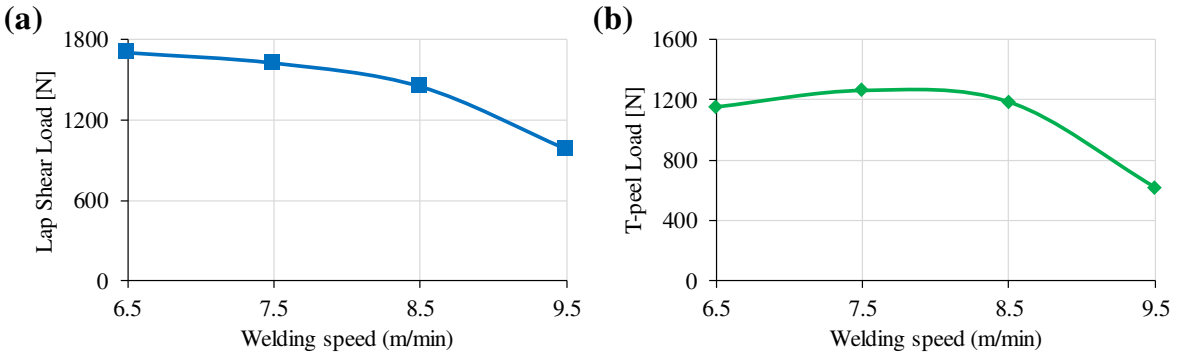

(c)

Welding Speed [m/min]	Maximum Lap shear Strength [N]		Maximum T-peel Strength [N]	
	Average	SD	Average	SD
6.5	1701.46	72.90	1154.09	80.30
7.5	1623.86	112.30	1263.21	193.74
8.5	1448.75	174.94	1186.48	134.55
9.5	981.27	123.80	618.75	155.51

Figure 8 Blue laser welded joint strength characterisation (a) lap shear load, (b) T-peel load, and (c) corresponding load average and standard deviation.

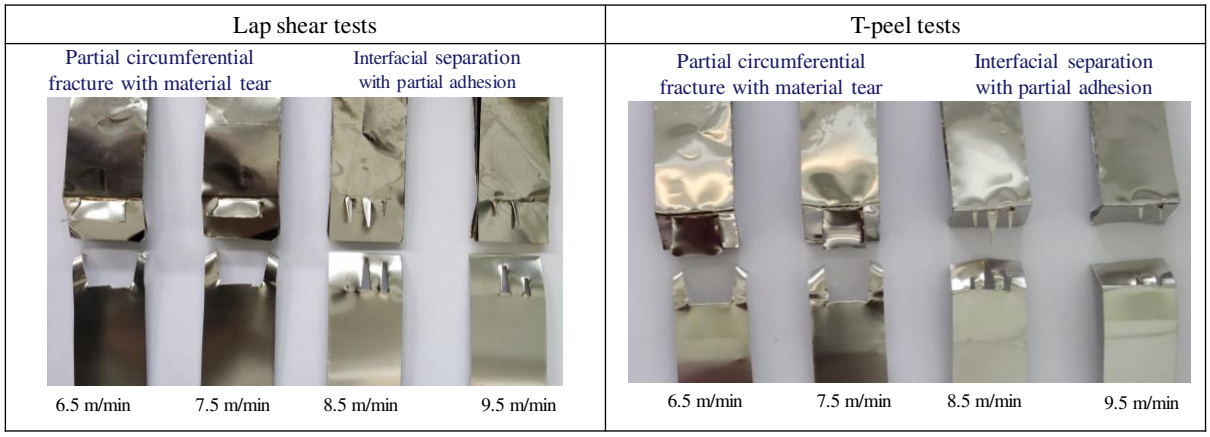

Figure 9 Failure modes obtained from the lap shear and T-peel tests.

4. Conclusions

This paper investigated, for the first time, the feasibility of laser welding multiple layers of thin stainless steel foils with the blue laser of ~450 nm wavelength. The results obtained from this study demonstrated that it is possible to produce multi-layered (i.e. 20 × 25 µm multiple micro-foils to 200 µm single foil) AISI 316L stainless steel joints. Microstructural and mechanical reliability can be achieved by precise control of blue laser energy input through variation of the welding speed. Based on the results obtained in this study, the following observations can be made:

- Joint fusion zone characteristics confirmed that the keyhole formation and depth of penetration could be easily controlled using blue laser welding where over-weld, good-weld and under-weld were categorised based on key geometrical characteristics.

- High-speed welding can be achieved using the blue laser as per the industrial requirement for high throughput.
- The suitability of blue laser welding for electrical micro joining involved the non-occurrence of welding cracks with little or no porosity within the fusion zone and low spatter.
- Epitaxial grain growth in the form of elongated columnar grains was obtained within the fusion zone as a result of the high cooling rate and directional cooling.
- The effects of microstructural heterogeneities in the fusion zone, heat affected zone and base material were mapped using microhardness profiles.
- In addition, the joint strength and preferred failure mode (i.e. partial circumferential fracture with material tear) were identified for good-welds.

In conclusion, this paper has demonstrated the suitability of blue laser welding for the joining of multiple thin foil layers in future energy storage applications. Furthermore, to quantify the advantages over IR laser, an in-depth comparison with detailed microstructural evaluation is proposed as future work.

Acknowledgements

This research is partially supported by Research and Development Fund (RDF) from the University of Warwick, NUBURU Inc. with laser experimental trials, and WMG Centre High Value Manufacturing (HVM) Catapult for characterisation and testing.

Reference

[1] V.A. Ventrella, J.R. Berretta, W. de Rossi, Pulsed Nd:YAG laser seam welding of AISI 316L stainless steel thin foils, Journal of Materials Processing Technology 210(14) (2010) 1838-1843.
[2] N. Abe, Y. Funada, T. Imanaka, M. Tsukamoto, Micro welding of thin stainless steel foil with a direct diode laser, Transactions of JWRI 34(1) (2005) 19-23.
[3] M.M. Thackeray, C. Wolverton, E.D. Isaacs, Electrical energy storage for transportation—approaching the limits of, and going beyond, lithium-ion batteries, Energy & Environmental Science 5(7) (2012) 7854-7863.
[4] A. Das, D. Li, D. Williams, D. Greenwood, Weldability and shear strength feasibility study for automotive electric vehicle battery tab interconnects, Journal of the Brazilian Society of Mechanical Sciences and Engineering 41(1) (2019) 54.
[5] E. Commission, Reducing CO2 emissions from passenger cars, 2017. https://ec.europa.eu/clima/policies/transport/vehicles/cars_en#tab-0-0. (Accessed 25-03-2017).
[6] E. Commission, Road transport: Reducing CO2 emissions from vehicles Policy. https://ec.europa.eu/clima/policies/transport/vehicles_en#tab-0-1. (Accessed 25/11/2019).
[7] A. Das, T.R. Ashwin, A. Barai, Modelling and characterisation of ultrasonic joints for Li-ion batteries to evaluate the impact on electrical resistance and temperature raise, Journal of Energy Storage 22 (2019) 239-248.
[8] A. Burke, Ultracapacitors: why, how, and where is the technology, Journal of Power Sources 91(1) (2000) 37-50.
[9] D.P. Dubal, O. Ayyad, V. Ruiz, P. Gómez-Romero, Hybrid energy storage: the merging of battery and supercapacitor chemistries, Chemical Society Reviews 44(7) (2015) 1777-1790.
[10] A. Das, A. Barai, I. Masters, D. Williams, Comparison of tab-to-busbar ultrasonic joints for electric vehicle Li-ion battery applications, World Electric Vehicle Journal 10(3) (2019) 55.

[11] R.B. Waghmode, H.S. Jadhav, K.G. Kanade, A.P. Torane, Morphology-controlled synthesis of NiCo2O4 nanoflowers on stainless steel substrates as high-performance supercapacitors, Materials Science for Energy Technologies 2(3) (2019) 556-564.
[12] A. Das, D. Li, D. Williams, D. Greenwood, Joining Technologies for Automotive Battery Systems Manufacturing, World Electric Vehicle Journal 9(2) (2018) 22.
[13] Y. Maletin, N. Strizhakova, S. Kozachkov, A. Mironova, S. Podmogilny, V. Danilin, J. Kolotilova, V. Izotov, J. Cederström, S.G. Konstantinovich, Supercapacitor and a method of manufacturing such a supercapacitor, Google Patents, 2003.
[14] S.S. Lee, T.H. Kim, S.J. Hu, W.W. Cai, J.A. Abell, Joining Technologies for Automotive Lithium-Ion Battery Manufacturing: A Review, ASME 2010 International Manufacturing Science and Engineering Conference, Pennsylvania, USA, 2010, pp. 541-549.
[15] A. Das, I. Masters, D. Williams, Process robustness and strength analysis of multi-layered dissimilar joints using ultrasonic metal welding, Int J Adv Manuf Technol 101(1) (2019) 881-900.
[16] S. Dhara, A. Das, Impact of ultrasonic welding on multi-layered Al–Cu joint for electric vehicle battery applications: A layer-wise microstructural analysis, Materials Science and Engineering: A 791 (2020) 139795.
[17] V. Dimatteo, A. Ascari, A. Fortunato, Continuous laser welding with spatial beam oscillation of dissimilar thin sheet materials (Al-Cu and Cu-Al): Process optimization and characterization, Journal of Manufacturing Processes 44 (2019) 158-165.
[18] U.F. Shaikh, A. Das, A. Barai, I. Masters, Electro-Thermo-Mechanical Behaviours of Laser Joints for Electric Vehicle Battery Interconnects, 2019 Electric Vehicles International Conference (EV), IEEE, 2019, pp. 1-6.
[19] M.S. Sa, M. Finuf, R. Fritz, J. Tucker, J.-M. Pelaprat, M.S. Zediker, Blue laser diode (450 nm) systems for welding copper, SPIE2018.
[20] J.P. Davim, Nontraditional machining processes, Manufacturing process selection handbook (2013) 205-226.
[21] R. Indhu, V. Vivek, L. Sarathkumar, A. Bharatish, S. Soundarapandian, Overview of Laser Absorptivity Measurement Techniques for Material Processing, Lasers in Manufacturing and Materials Processing 5(4) (2018) 458-481.
[22] N. Tepylo, X. Huang, P.C. Patnaik, Laser-Based Additive Manufacturing Technologies for Aerospace Applications, Advanced Engineering Materials 21(11) (2019) 1900617.
[23] J.-M. PELAPRAT, M. FINUF, E. BOESE, M. ZEDIKER, Blue lasers add power and brightness, 2020. https://www.industrial-lasers.com/welding/article/14173138/blue-lasers-add-power-and-brightness. (Accessed 08/06/2020).
[24] M. Zediker, R. Fritz, M. Finuf, J. Pelaprat, Laser welding components for electric vehicles with a high-power blue laser system, Journal of Laser Applications 32(2) (2020) 022038.
[25] J. Kell, J. Tyrer, R. Higginson, R. Thomson, Microstructural characterization of autogenous laser welds on 316L stainless steel using EBSD and EDS, Journal of microscopy 217(2) (2005) 167-173.
[26] M. Jandaghi, P. Parvin, M.J. Torkamany, J. Sabbaghzadeh, Alloying element losses in pulsed Nd : YAG laser welding of stainless steel 316, Journal of Physics D: Applied Physics 41(23) (2008) 235503.
[27] N. Kumar, M. Mukherjee, A. Bandyopadhyay, Comparative study of pulsed Nd:YAG laser welding of AISI 304 and AISI 316 stainless steels, Optics & Laser Technology 88 (2017) 24-39.
[28] P. Saha, D. Waghmare, Parametric optimization for autogenous butt laser welding of sub-millimeter thick SS 316 sheets using central composite design, Optics & Laser Technology 122 (2020) 105833.
[29] V.A. Ventrella, J.R. Berretta, W. De Rossi, Application of pulsed Nd: YAG laser in thin foil microwelding, International Journal of Materials and Product Technology 48(1-4) (2014) 194-204.
[30] J. Kim, S. Kim, K. Kim, W. Jung, D. Youn, J. Lee, H. Ki, Effect of beam size in laser welding of ultra-thin stainless steel foils, Journal of Materials Processing Technology 233 (2016) 125-134.
[31] M.R. Pakmanesh, M. Shamanian, Optimization of pulsed laser welding process parameters in order to attain minimum underfill and undercut defects in thin 316L stainless steel foils, Optics & Laser Technology 99 (2018) 30-38.
[32] Advent Research Materials. https://www.advent-rm.com/catalogue/stainless-steel-aisi-316/foil/FE6944/. (Accessed 14/04/2019).

[33] R. Akhter, W. Steen, The gap model for welding zinc-coated steel sheet, Proceedings of the International Conference on Lasers Systems Application in Industry, Torino, Italy, 1990, pp. 219-236.
[34] A. Das, P. Franciosa, D. Ceglarek, Fixture design optimisation considering production batch of compliant non-ideal sheet metal parts, Procedia Manufacturing 1 (2015) 157-168.
[35] B.E.I. 6892-1:2019, Metallic materials. Tensile testing. Method of test at room temperature, BSI Standards Publication, 2019.
[36] M. Keskitalo, J. Sundqvist, K. Mäntyjärvi, J. Powell, A.F.H. Kaplan, The Influence of Shielding Gas and Heat Input on the Mechanical Properties of Laser Welds in Ferritic Stainless Steel, Physics Procedia 78 (2015) 222-229.
[37] P.A. Molian, Solidification behaviour of laser welded stainless steel, Journal of Materials Science Letters 4(3) (1985) 281-283.
[38] T. Sun, A.P. Reynolds, M.J. Roy, P.J. Withers, P.B. Prangnell, The effect of shoulder coupling on the residual stress and hardness distribution in AA7050 friction stir butt welds, Materials Science and Engineering: A 735 (2018) 218-227.